

Controlling complex dynamics with synthetic magnetism in optomechanical systems: A route to enhanced sensor performance

Deivasundari Muthukumar¹, Stella Rolande Mbokop Tchounda², Sifeu Takougang Kingni^{3,*}, Karthikeyan Rajagopal^{1,4}, and Serge Guy Nana Engo²

¹*Center for research, SRM Easwari Engineering College, Chennai 600 089, India*

²*Department of Physics, Faculty of Sciences, University of Yaoundé I, P.O. Box 812, Yaoundé, Cameroon*

³*Department of Mechanical, Petroleum and Gas Engineering, National Advanced School of Mines and Petroleum Industries, University of Maroua, P.O. BOX 46, Maroua, Cameroon*

⁴*Center for Cognitive Science, Trichy SRM Medical College Hospital and Research Center, Tamil Nadu 621 105, India*

* *Corresponding author: sifeu.takougang@facsciences-uy1.cm, stkingni@gmail.com*

Abstract

This paper explores the intricate dynamical behavior of an optomechanical system consisting of an optical resonator that drives two mechanically coupled resonators via phase-dependent phonon hopping. Addressing previous limitations in comprehending the dynamics of such systems, we derive the system's semiclassical dynamical equations from the optomechanical Hamiltonian, resulting in a set of six first-order ordinary differential equations. We subsequently illustrate the emergence of novel dynamic behaviors and demonstrate their pertinence for the development of new devices. The system exhibits either two or no steady states, contingent upon the incident radiation, mechanical coupling rate, and frequency detuning. Our stability analysis indicates that the stability of these states is determined by the same factors. We identify complex dynamical behaviors, including monostable and bistable self-excited quasi-periodic characteristics, the coexistence of hidden oscillations, and chaotic dynamics, and we propose a method for their control. These findings bear significant implications for applications in ultra-sensitive sensing, chaos-based communication, and tunable phononic circuits. This study enhances the broader understanding of complex dynamical systems in optomechanics, paving the way for the development of advanced optomechanical devices with controlled dynamics for stable and reliable operation.

Keywords: Optomechanics, Nonreciprocal Interactions, Synthetic Gauge Fields, Bistability, Chaos-Based Sensing

1 Introduction

Optomechanics explores the intricate interactions between light and mechanical systems, where optical fields manipulate mechanical vibrations, which, in turn, influence the optical properties of the system [1]. This dual interaction facilitates a wide array of applications, including precision metrology [2], quantum information technologies [3, 4], and the creation of highly sensitive sensors [5].

This study aims to enhance optomechanical systems by investigating innovative control mechanisms and functionalities. A particularly promising avenue for advancement is the integration of non-Hermitian physics [6, 7], parity-time (PT) symmetry [8], and synthetic magnetism [9]. Non-Hermitian systems, characterized by their capability to dissipate energy due to their open quantum nature, facilitate the occurrence of exceptional points (EPs), which are non-Hermitian degeneracies where modes coalesce in both resonance frequency and decay rate [10–12]. These exceptional points exhibit distinctive properties, thereby enabling their application across various domains [13–15]. Conversely, synthetic magnetism involves the generation of artificial magnetic fields within neutral systems, effectively emulating the influence of real magnetic fields on charged particles.

Recent advancements in the realm of synthetic magnetism within optomechanical systems have predominantly relied upon exceptional points and PT symmetry as mechanisms to facilitate nonreciprocal phonon transport [16, 17]. In contrast, our methodology attains synthetic gauge fields without necessitating gain-loss frameworks, instead leveraging phase-dependent phonon hopping. This approach provides a platform that is both more stable and tunable for phononic circuits. However, such advancements are not universally guaranteed and often pose significant challenges in practical implementation.

Synthetic gauge fields and topological configurations unlock numerous possibilities for novel device architectures. The adoption of non-reciprocal devices, which permit wave propagation in a single direction, has been proposed for a broad range of applications. Nevertheless, a deeper insight into the association between synthetic magnetism and the ensuing dynamic behavior, particularly within the non-linear regime, remains essential. Although various studies have illustrated the application of synthetic magnetism in optomechanical systems [18, 19], a comprehensive examination addressing their implications on non-linear dynamics is necessary to fully unlock the potential of these systems for constructing new and robust devices.

Prior research has underscored the effectiveness of integrating PT symmetry and non-Hermitian principles in the manipulation of optical systems [14, 20, 21]. These investigations have illustrated the capability to create devices with functions such as unidirectional invisibility and enhanced sensing. Recent explorations have further considered topological configurations and synthetic gauge fields as tools for novel manipulations of light and sound [22]. Nonetheless, these studies frequently concentrated on static or linear regimes and exhibited constraints in examining the system's intricate dynamical behavior. Therefore, further exploration of how the tunability of synthetic magnetism can be exercised for robust control over non-linear dynamics and stability is critical for the applied utilization of such systems in real-world scenarios.

Addressing this research gap constitutes the core objective of this study. The principal research questions that will be addressed include: How can synthetic magnetism influence the dynamical behavior of optomechanical systems? What is the significance of phase-dependent phonon hopping in the formation of complex dynamic states, with prospective applications in quantum technologies? How do variations in system parameters affect the stability of the dynamic behavior in these devices, and can these techniques be employed to enhance the performance of optomechanical devices?

This paper presents an investigation into the dynamical characteristics of an optomechanical system consisting of an optical resonator that drives two mechanically coupled resonators via phase-dependent phonon hopping. Combining analytical and numerical methodologies, we examine the system's dynamics across red and blue detuning regimes and identify the conditions requisite for the realization of synthetic gauge fields, engineered through exceptional points, independently of amplification mechanisms. Our key findings include: (i) emergence of bistability and self-excited quasi-periodic oscillations, demonstrating the system's ability to support multiple steady states; (ii) identification of hidden attractors and chaotic regimes, revealing complex dynamical transitions that are highly sensitive to initial conditions; (iii) impact of synthetic magnetism on stability, showing how phase-dependent phonon hopping modulates nonreciprocal interactions and controls system dynamics. These results provide new insights into the design of tunable optomechanical systems, with potential applications in ultra-sensitive sensing, chaos-based communication, and phononic signal processing. The manuscript is structured as follows: In Section 2, the optomechanical system is characterized with its Hamiltonian, laying the groundwork for subsequent analyses. Section 3 details our methodology for investigating the dynamic behavior of the optomechanical system. Section 3 offers a presentation and discussion of our study's findings. Lastly, Section 4 summarizes the conclusions and perspectives emerging from this research.

2 System and methods

This section provides a detailed description of the optomechanical system under investigation and outlines the analytical and numerical methodologies utilized to examine its dynamical attributes and potential applications in sensor technology. Specifically, we expound upon the schematic, equations, and selected parameters.

2.1 Optomechanical system model

We consider an optomechanical system consisting of a single optical cavity driving two mechanically linked nanoresonators, each of which is independently driven by a coherent input field α_j^{in} . This configuration investigates the dynamics under a regime of enhanced dissipative coupling, characterized by

a tunable rate η that modulates cavity losses based on mechanical displacements. Mechanical coupling is introduced via a coupling force J_m between the resonators, enabling energy exchange. The system we employ, as illustrated in Figure 1, is based on the designs implemented in [23]. A significant feature of the system is the phase-dependent nature of J_m . Consequently, critical parameters such as stability, coherence, and the emergence of exceptional points (EPs) are intricately interconnected, depending on the phase.

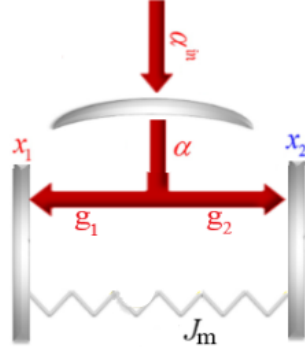


Figure 1: Illustration of the optomechanical configuration analyzed in this study. The setup comprises two mechanically coupled optomechanical resonators, where each resonator is individually driven by a coherent input field α_j^{in} . This configuration explores the dynamics under a regime of enhanced dissipative coupling, characterized by a tunable rate η that modulates cavity losses based on mechanical displacements. Mechanical coupling is introduced via a coupling force J_m between the resonators, enabling energy exchange. J_m is θ phase-dependent. The resonators are parametrically coupled to optical cavities whose resonance frequencies ω_{cav}^j are detuned by Δ_j from their respective input laser frequencies. The dissipative interaction is mediated by waveguides with an effective group index \bar{n}_g and a characteristic dissipation rate κ_x . This figure highlights key parameters influencing stability, coherence, and the emergence of exceptional points (EPs) within the system.

The choice of studying a two-resonator system is motivated by several considerations. Firstly, two-resonator systems represent the most straightforward configuration that allow for the exploration of non-trivial effects in coupled optomechanical systems, thereby rendering the system's physics more comprehensible. Additionally, preceding research has demonstrated the feasibility of developing efficient sensors with merely two resonators [23]. Exploring configurations with an increased number of resonators augments the system's complexity and may introduce superfluous challenges in the initial characterization of the system's properties. Consequently, the chosen system constitutes a straightforward approach to realize an effective model. The Hamiltonian is described below. For our simulation, we assumed the following parameters: $\omega_1 = \omega_m$, $\omega_2 = (1 + 5 \times 10^{-4})\omega_m$, $\kappa = 7.3 \times 10^{-2}\omega_m$, $\Delta = \omega_m$, $g = 1.077 \times 10^{-4}\omega_m$, $\gamma_1 = 1.077 \times 10^{-5}\omega_m$, $\gamma_2 = \gamma_1$, and $J_m = 2 \times 10^{-4}\omega_m$. These parameters were selected to ensure the system manifests measurable non-linear effects, as such effects necessitate strong coupling between the various components. Furthermore, this scaling sustains the system's dynamics while facilitating direct application to physical implementations [24]. For instance, employing these parameters with a pump power approximately around $130\sqrt{\omega_m}$ W yields an optical to mechanical energy ratio of about $0.1\omega_m$ W, which is deemed suitable. It is also imperative to acknowledge that these particular values, concerning ω_m , are contingent on the materials employed.

In order to ensure conformity with existing technological advancements, the parameters employed in our model are maintained within the confines of experimentally attainable thresholds. This consideration is based on the observation that optomechanical devices utilizing silicon nitride (SiN) and silicon-on-insulator (SOI) platforms exhibit analogous coupling rates and dissipation mechanisms [25, 26]. The subsequent section elaborates on these foundational elements to facilitate further scholarly advancements.

The practical implementation requires precise regulation of phase-dependent interactions, particularly in sustaining stability across diverse temperature conditions. Integrated microheaters, for instance, can be employed to adjust this phase. To guarantee thermal stability and mitigate phase drift over time, their integration with temperature control systems, such as cryogenic cooling, may be required. The experimental demonstration of synthetic gauge fields through engineered optomechanical couplings was conducted using silicon nitride (SiN) optomechanical resonators by Lawrie *et al.* [26], whereas Fang *et al.* [27] introduced a novel approach to illustrate the significance of non-reciprocity by utilizing

phonon transport in these systems. As an enhancement strategy, phase-dependent phonon hopping can be experimentally regulated via integrated heaters or optomechanical parametric driving. Nonetheless, challenges such as phase drift due to fabrication imperfections, ambient noise, and material inhomogeneities must be addressed to preserve coherence. High-precision nanofabrication techniques, including electron-beam lithography and atomic layer deposition, can assist in minimizing structural asymmetries, thereby ensuring robust performance in real-world applications.

Recent experimental investigations have further substantiated the feasibility of phase-dependent phonon hopping within optomechanical systems. Specifically, Ren *et al.* [28] demonstrated that through meticulous engineering of mechanical coupling and optical drive phases, nonreciprocal phonon transport can be realized in integrated optomechanical resonators. This experimental corroboration enhances the feasibility of implementing the synthetic gauge fields examined in this study utilizing advanced nanofabrication techniques. Consequently, using appropriate experimental components is advantageous for validating the findings presented herein and is also important for the practical application of this methodology.

2.2 System Hamiltonian

The system Hamiltonian, under the rotating-wave approximation and in a frame rotating at the driving laser frequency ω_p , is given by (under the assumption $\hbar = 1$):

$$\hat{H} = \hat{H}_O + \hat{H}_M + \hat{H}_{OM} + \hat{H}_{MM} + \hat{H}_{\text{drive}} + \hat{H}_{\text{diss}}, \quad (1)$$

where each term describes a different aspect of the optomechanical system:

- $\hat{H}_O = -\Delta \hat{a}^\dagger \hat{a}$ denotes the energy within the optical cavity, with $\Delta = \omega_p - \omega_{\text{cav}}$ indicating the detuning between the frequency of the driving laser ω_p and the cavity's resonance frequency ω_{cav} . This energy is contingent upon the photons number within the cavity and the detuning relative to the external driving laser, which collectively influence the potential stability of the cavity state. A lower value in this parameter suggests a stable state of operation, potentially minimizing noise and enhancing sensor efficiency.
- $\hat{H}_M = \sum_{j=1,2} \omega_j \hat{b}_j^\dagger \hat{b}_j$ represents the energy of the two mechanical resonators, where ω_j refers to the resonance frequency of the j^{th} resonator and \hat{b}_j signifies the corresponding annihilation operator. The use of two mechanical resonators was selected due to its status as the simplest arrangement that allows for the examination of complex dynamics, consequently leading to novel non-reciprocal effects. This investigation focuses on two resonators, although one can consider coupling with additional resonators to harness collective phenomena within this system. In each mechanical resonator, energy is assumed to be quantized using bosonic operators, as the mechanical frequency is lower than the thermal energy, ensuring the presence of multiple quanta in the mechanical modes.
- $\hat{H}_{OM} = \sum_{j=1,2} -g_j \hat{a}^\dagger \hat{a} (\hat{b}_j^\dagger + \hat{b}_j)$ denotes the energy associated with the optomechanical interaction, where g_j signifies the single-photon optomechanical coupling strength between the cavity mode and the j^{th} mechanical resonator. This term describes the reciprocal effect that photons within the optical cavity and the mechanical resonators exert upon each other. The optomechanical coupling rates can be realized by employing materials with substantial optomechanical coefficients, such as Si or SiN [25], and are contingent upon factors such as the optical power and frequency deployed in the cavities, the mechanical resonator's geometry and material, as well as its mass and size. This term is pivotal in delineating the relationship between the mechanical and optical properties, necessitating that the system be engineered to optimally utilize this value within the context of the coupling process.
- $\hat{H}_{MM} = J_m (e^{i\theta} \hat{b}_1^\dagger \hat{b}_2 + e^{-i\theta} \hat{b}_1 \hat{b}_2^\dagger)$ characterizes the mechanical coupling between the two resonators. Here, J_m represents the mechanical coupling rate, while θ indicates the coupling phase, which facilitates the construction of synthetic gauge fields. The phase-dependent nature of this coupling permits the realization of chiral or non-reciprocal interactions, thus affording a heightened level of control over system dynamics. By modulating the phase, the energy transfer direction between the resonators can be altered. This phase is externally regulated, for example, by incorporating integrated heaters to induce thermal expansion within the resonators. While the specific value of the coupling does not critically impact our study, provided the resonators remain coupled, exceedingly high mechanical coupling can lead to system destabilization. Various methodologies exist

for achieving this coupling, with the direct, spring-like coupling configuration drawing direct inspiration from nano-optomechanical systems [26] or even from macroscopic optomechanical systems, which have been employed to monitor quantum phenomena. Furthermore, the interplay between such mechanical coupling and zero-point fluctuations constitutes another design consideration for these systems.

- $\hat{H}_{\text{drive}} = i\sqrt{\kappa}\alpha^{\text{in}}(\hat{a}^\dagger - \hat{a})$ elaborates on the excitation of the optical cavity via an external laser field. κ represents the cavity decay rate, assumed identical across both cavities, while α^{in} denotes the driving amplitude. We posit that the two mechanical resonators exhibit comparable characteristics and are coupled with identical parameters to the same driving laser. Additionally, we assume both resonators possess equivalent zero-point fluctuations and are similar in dimension. This value ultimately dictates the power input into our system, requisite for the observation of quantum phenomena, and must therefore be calibrated neither excessively high nor low relative to the optomechanical rate. The parameters governing the laser driving are contingent upon the available system, thus constraining our selection to the experimental limitations. The laser frequency must also demonstrate stability. This driving field serves to inject energy into the system, which subsequently has the potential to dissipate as heat through interaction with the environment. It is imperative for the energy input to exceed the dissipation rate.
- \hat{H}_{diss} accounts for the dissipative elements, encompassing both optical and mechanical dissipation, which are influenced by thermal noise. Specifically, dissipation transpires as the system engages with the surrounding environment. We anticipate that both the temperature and environmental interaction will correlate with the size and thermal properties of the components, thereby imposing configuration constraints. The dissipation terms are expressed as:

$$\hat{H}_{\text{diss}} = i\sqrt{\kappa}(\hat{a}^\dagger a_{\text{in}} - \hat{a}\hat{a}_{\text{in}}^\dagger) + i \sum_{j=1,2} \sqrt{\gamma_j}(\hat{b}_j^\dagger b_{j,\text{in}} - \hat{b}_j b_{j,\text{in}}^\dagger) \equiv \hat{H}_\kappa + \hat{H}_\gamma, \quad (2)$$

where γ_j signifies the damping rate of the mechanical resonator j , and \hat{a}_{in} and $\hat{b}_{j,\text{in}}$ represent the input noise operators. This Hamiltonian is crucial for achieving more precise outcomes, as well as enabling the energy to channel into specific domains when system behavior displays chaotic characteristics.

2.3 Dynamical equations

To derive the dynamics of the system, we employ the Heisenberg-Langevin equations

$$\frac{d\hat{O}}{dt} = i[\hat{H}, \hat{O}] + \hat{N}, \quad (3)$$

where \hat{O} represents the system operators (\hat{a} , \hat{b}_1 , \hat{b}_2) and $\hat{N} \equiv (\hat{a}_j^{\text{in}}, \hat{b}_j^{\text{in}})$ is the corresponding noise operator. In detail, this means that we replace each of the operators in turn as follows: $\hat{O} \rightarrow \hat{a}, \hat{b}_1, \hat{b}_2$. We then can obtain the following set of equations:

$$\dot{\hat{a}} = \left(i\Delta - \frac{\kappa}{2}\right)\hat{a} + \sum_{j=1,2} ig_j(\hat{b}_j^\dagger + \hat{b}_j)\hat{a} + \sqrt{\kappa}\hat{a}^{\text{in}}, \quad (4a)$$

$$\dot{\hat{b}}_1 = -\left(i\omega_1 + \frac{\gamma_1}{2}\right)\hat{b}_1 - iJ_m e^{i\theta}\hat{b}_2 - ig_1\hat{a}^\dagger\hat{a} + \sqrt{\gamma_1}\hat{b}_1^{\text{in}}, \quad (4b)$$

$$\dot{\hat{b}}_2 = -\left(i\omega_2 + \frac{\gamma_2}{2}\right)\hat{b}_2 - iJ_m e^{-i\theta}\hat{b}_1 - ig_2\hat{a}^\dagger\hat{a} + \sqrt{\gamma_2}\hat{b}_2^{\text{in}}. \quad (4c)$$

2.3.1 Linearization of quantum Heisenberg-Langevin equations

To analyze the system's behavior, the nonlinear QLEs are linearized. Operators \mathcal{O} are decomposed into steady-state values $\langle \mathcal{O} \rangle \equiv (\beta_j, \alpha_j)$ and small fluctuations $\delta\mathcal{O} \equiv (\delta\beta_j, \delta\alpha_j)$ as follows:

$$\mathcal{O} = \langle \mathcal{O} \rangle + \delta\mathcal{O}. \quad (5)$$

The averaged dynamical equations can be expressed as:

$$\dot{\alpha} = (i\tilde{\Delta} - \frac{\kappa}{2})\alpha + \sqrt{\kappa}\alpha^{\text{in}}, \quad (6a)$$

$$\dot{\beta}_1 = -(i\omega_1 + \frac{\gamma_1}{2})\beta_1 - iJ_m e^{i\theta}\beta_2 - ig_1|\alpha|^2, \quad (6b)$$

$$\dot{\beta}_2 = -(i\omega_2 + \frac{\gamma_2}{2})\beta_2 - iJ_m e^{-i\theta}\beta_1 - ig_2|\alpha|^2. \quad (6c)$$

Additionally, the time-dependent zero-mean fluctuation dynamical equations are given by:

$$\delta\dot{a} = \left(i\tilde{\Delta} - \frac{\kappa}{2}\right)\delta a - i\sum_j g_j(\delta\hat{b}_j^\dagger + \delta\hat{b}_j)\alpha + \sqrt{\kappa}a^{\text{in}}, \quad (7a)$$

$$\delta\dot{b}_1 = -(i\omega_1 + \frac{\gamma_1}{2})\delta b_1 - iJ_m e^{i\theta}\delta b_2 - ig_1(\alpha^\dagger\delta a + \alpha\delta a^\dagger) + \sqrt{\gamma_1}b_1^{\text{in}}, \quad (7b)$$

$$\delta\dot{b}_2 = -(i\omega_2 + \frac{\gamma_2}{2})\delta b_2 - iJ_m e^{-i\theta}\delta b_1 - ig_2(\alpha^\dagger\delta a + \alpha\delta a^\dagger) + \sqrt{\gamma_2}b_2^{\text{in}}. \quad (7c)$$

Here, $\tilde{\Delta} = \Delta - 2g_1\Re(\beta_1) - 2g_2\Re(\beta_2)$ represents the effective detuning, and $G_j = g_j\alpha$ denotes the effective many photon optomechanical coupling strength.

We considered that second-order fluctuations $\delta a\delta a$, $\delta\hat{b}_j\delta\hat{b}_j$ and $\delta\hat{b}_j\delta a$ are very small quantities and can thus be neglected. Additionally, we have $\alpha^*\alpha = |\alpha|^2$, which tends towards the number of photons, and $\alpha^* = \alpha$ in the linear regime. For convenience, we adopt a real/imaginary decomposition $\alpha = \alpha_r + i\alpha_i$ and $\beta_j = \beta_{jr} + i\beta_{ji}$, where α_r , β_{jr} are the real parts and α_i , β_{ji} are the imaginary parts, respectively. Consequently, the set of equations in (8) becomes:

$$\frac{d\alpha_r}{dt} = -(\Delta - 2g_1\beta_{1r} - 2g_2\beta_{2r})\alpha_i - \frac{\kappa}{2}\alpha_r + \sqrt{\kappa}\alpha^{\text{in}}, \quad (8a)$$

$$\frac{d\alpha_i}{dt} = (\Delta - 2g_1\beta_{1r} - 2g_2\beta_{2r})\alpha_r - \frac{\kappa}{2}\alpha_i, \quad (8b)$$

$$\frac{d\beta_{1r}}{dt} = \omega_1\beta_{1i} - \frac{\gamma_1}{2}\beta_{1r} + J_m(\beta_{2r}\sin\theta + \beta_{2i}\cos\theta), \quad (8c)$$

$$\frac{d\beta_{1i}}{dt} = -\omega_1\beta_{1r} - \frac{\gamma_1}{2}\beta_{1i} - J_m(\beta_{2r}\cos\theta - \beta_{2i}\sin\theta) - g_1(\alpha_r^2 + \alpha_i^2), \quad (8d)$$

$$\frac{d\beta_{2r}}{dt} = \omega_2\beta_{2i} - \frac{\gamma_2}{2}\beta_{2r} - J_m(\beta_{1r}\sin\theta - \beta_{1i}\cos\theta), \quad (8e)$$

$$\frac{d\beta_{2i}}{dt} = -\omega_2\beta_{2r} - \frac{\gamma_2}{2}\beta_{2i} - J_m(\beta_{1r}\cos\theta + \beta_{1i}\sin\theta) - g_2(\alpha_r^2 + \alpha_i^2). \quad (8f)$$

2.3.2 Stability analysis

The equilibrium points of the system are determined by setting $\dot{\alpha} = 0$ and $\dot{\beta}_j = 0$. These steady-state values can be expressed as:

$$\beta_1 = -\frac{2(2g_2J_m e^{i\theta} + ig_1\gamma_2 - 2g_1\omega_2)|\alpha|^2}{4J_m^2 - 4\omega_1\omega_2 + 2i(\gamma_1\omega_2 + \gamma_2\omega_1) + \gamma_1\gamma_2}, \quad \beta_2 = -\frac{2(2g_1J_m e^{-i\theta} + ig_2\gamma_1 - 2g_2\omega_1)|\alpha|^2}{4J_m^2 - 4\omega_1\omega_2 + 2i(\gamma_1\omega_2 + \gamma_2\omega_1) + \gamma_1\gamma_2}. \quad (9)$$

where the steady-state amplitude of the optical field is given by:

$$a_r = \frac{2\alpha^{\text{in}}}{\sqrt{\kappa}}, \quad (10)$$

and a_i is obtained from the quadratic equation:

$$A_0 a_i^2 + A_1 a_i + A_2 = 0, \quad (11)$$

where the coefficients are:

$$A_0 = 32\alpha^{\text{in}}\kappa[\cos\theta g_1 g_2 J_m (8J_m^2 + 2\gamma_1 \gamma_2 - 8\omega_1 \omega_2) - 4J_m^2 g_1^2 \omega_2 - 4J_m^2 g_2^2 \omega_1 + g_1^2 \gamma_2^2 \omega_1 + 4g_1^2 \omega_1 \omega_2^2 + g_2^2 \gamma_1^2 \omega_2 + 4g_2^2 \omega_1^2 \omega_2], \quad (12a)$$

$$A_1 = -\kappa^{5/2}(16J_m^2 + 8J_m^2 \gamma_1 \gamma_2 - 32J_m^2 \omega_1 \omega_2 + \gamma_1^2 \gamma_2^2 + 4\gamma_1^2 \omega_2^2 + 4\gamma_2^2 \omega_1^2 + 16\omega_1^2 \omega_2^2), \quad (12b)$$

$$A_2 = 4(\alpha^{\text{in}})^2 [256J_m^3 \cos\theta g_1 g_2 \gamma_1 + 64J_m \cos\theta g_1 g_2 \gamma_1 \gamma_2 \kappa + 8\Delta J_m^2 \gamma_1 \gamma_2 \kappa - 32\Delta J_m^2 \omega_1 \omega_2 \kappa + \Delta \gamma_1^2 \gamma_2^2 \kappa - 256J_m \cos\theta g_1 g_2 \omega_1 \omega_2 \kappa - 128J_m^2 g_1^2 \omega_2 \kappa + 128g_2^2 \omega_2 \omega_1^2 (\alpha^{\text{in}})^2 - 128J_m^2 g_2^2 \omega_1 \kappa + 16\Delta J_m^4 \kappa - 8\Delta J_m^2 \gamma_1 \gamma_2 \kappa + 32\Delta g_1^2 \omega_1 \omega_2^2 (\alpha^{\text{in}})^2 + 32g_2^2 \gamma_1^2 \omega_2 (\alpha^{\text{in}})^2 - 32\Delta J_m^2 \omega_1 \omega_2 \kappa + \Delta \gamma_1^2 \gamma_2^2 \kappa + 4\Delta \gamma_1^2 \omega_2^2 \kappa + 4\Delta \omega_1^2 \gamma_2^2 \kappa + 16\Delta \omega_1^2 \omega_2^2 \kappa]. \quad (12c)$$

To ascertain the stability of equilibrium points, the Routh-Hurwitz criterion is employed. This criterion guarantees that all roots of the characteristic polynomial possess negative real parts. Despite its limited robustness, it is the most straightforward method and enjoys extensive application. A system is deemed stable if its imaginary components do not exhibit exponential growth over time. The linearized system, along with its stability attributes, merely offers a preliminary insight into stability conditions. The most accurate characterization of the complex dynamics inherent in the optomechanical system is still achieved through the analysis of the original system's equations of motion.

Although the Routh-Hurwitz criterion provides a preliminary approach to stability assessment, it does not capture transitions into quasiperiodic or chaotic states. For a more comprehensive examination of the system's stability, Floquet analysis might be utilized for periodic attractors [29], while Lyapunov exponents can quantify chaos in scenarios where the system demonstrates sensitive dependence on initial conditions. Furthermore, bifurcation diagrams illustrating stability loss with varying J_m and Δ parameters offer insights into system dynamics. Despite these limitations, this study employs the Routh-Hurwitz criterion as a practical tool that approximates the range of values indicative of stable behavior while also simplifying the complexity of the problem.

3 Results and discussion

This section investigates the intricate and nuanced dynamics of the system, including the emergence of bistability, along with an examination of the influence exerted by the mechanical coupling rate and frequency detuning. The findings derived from this analysis serve as a foundational framework for addressing challenges associated with limited dynamic range and provide insights into how the integration of multiple resonators impacts the performance of sensors. Furthermore, this section evaluates the potential applications of the system in domains such as signal processing and communications based on chaotic dynamics. The semiclassical dynamical equations, derived from the Hamiltonian of the optomechanical system, were reformulated into a set of six first-order ordinary differential equations through the real/imaginary decomposition method delineated in Eq. (8). This six-dimensional system is subject to numerical study.

3.1 Stability basins

The demarcation of stability basins defines the explicit boundaries delineating zones for various steady states within the parameter space. Considering the inherent limitations posed by a restricted dynamic range and heightened sensitivity to external perturbations, there is a pressing need for utilizing stable regions to construct robust and reliable systems. Consequently, a thorough understanding of these stability basins is essential for the design of practical devices. These regions specify the conditions under which a device can function reliably and controllably, ultimately influencing the sensitivity and usability of the device in empirical experiments. Furthermore, the application of the Routh-Hurwitz criterion elucidates the spectrum of reliable systems, facilitating the development of less complex and more user-friendly devices.

In Figure 2, the regions within the parameter space delineating the number of steady states manifested by the system are observed. Cyan dots denote zones devoid of steady states, whereas blue dots signal the presence of two steady states. With an escalation in parameter α^{in} , there is a diminished presence of regions with two steady states, giving rise to an expansion of domains with no steady states. Specifically, when parameter α^{in} exceeds a critical threshold ($\alpha^{\text{in}} = 100$), the regions of two steady states vanish completely, thereby leaving only those without steady states. A practical repercussion of this transition is

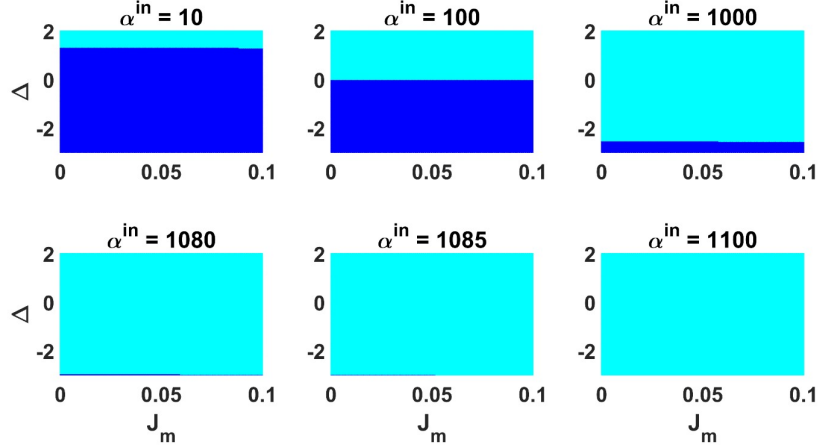


Figure 2: Phase diagram showing the number of steady states in the (Δ, J_m) parameter space as the input power α^{in} varies. Cyan dots mark regions where no steady states exist, while blue dots denote regions with two coexisting steady states. This analysis reveals how variations in α^{in} influence the existence of multiple steady states and delineates the range of mechanical coupling values supporting bistability.

the system’s inability to function as a bistable device—such as in optical switches or memory elements—at the values of $\alpha^{\text{in}} > 1100$. This limitation requires the exploration of alternative architectures to sustain applications requiring operation over extended durations with a robust steady state.

The transition arises from a bifurcation in the system’s dynamics, where distinct attractors collapse and disappear. Such bifurcations offer avenues for controlling system behavior; however, they might also induce undesirable effects like transient oscillations or instability if not understood thoroughly. This highlights the imperative of precise parameter control within the system to sidestep chaotic or unstable regimes. Conversely, for other applications, harnessing the onset of chaos can be advantageous, such as in chaos-based communication, where heightened sensitivity to parameter variations is not a liability but rather a rationale for selecting that method. This outcome is pivotal for subsequent experimentation with these materials, as the values for J_m and temperature must be carefully selected to render the device functional.

The characteristic polynomial of the system, denoted as $S(a_r, a_i, b_{1r}, b_{1i}, b_{2r}, b_{2i})$, is expressed as:

$$\lambda^6 + c_1\lambda^5 + c_2\lambda^4 + c_3\lambda^3 + c_4\lambda^2 + c_5\lambda + c_6 = 0. \quad (13)$$

In accordance with the Routh-Hurwitz criteria, the steady states are considered stable if the real components of the complex eigenvalues obtained from the characteristic polynomial (13) are negative. In the design of devices predicated on such systems, an understanding of these stability regions facilitates the precise adjustment of the parameters of the system, thereby ensuring operation within stable regimes.

The stability of these steady states is further examined in Figure 3, where we illustrate the variation in stability across different parameter values. The first row panels in Figure 3 depict the stability of the first steady state, whereas the second row panels pertain to the second steady state. In this context, black dots denote regions of stable steady states, while red dots indicate regions of unstable states. This extensive analysis unveils the intricate relationship between the system parameters and its dynamical behavior, forming a foundation for the study of the complex interactions within the optomechanical system. The existence of stable, coexisting steady states can be harnessed to construct optical switches, where distinct states can correspond to varying states of light transmission, or as memory elements endowed with robust properties. Nonetheless, the presence of these multiple steady states can pose challenges, necessitating precise control of the parameter regimes to preclude undesired transitions between states.

Given that Figure 2 demonstrates that the system defined by Eq. (8) exhibits two steady states for certain parameter values ($\alpha^{\text{in}} \leq 1000$) and no steady state for others ($\alpha^{\text{in}} \geq 1100$), it becomes imperative to investigate the dynamical characteristics of the system across the parameter space delineated by the mechanical coupling rate J_m and the frequency detuning Δ . The existence of such complex attractors can be leveraged to regulate information flow in optomechanical networks, as in chaos-based communication.

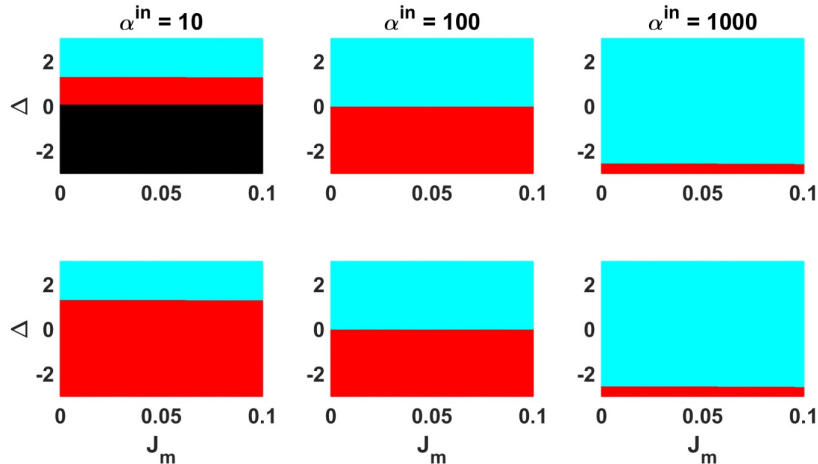


Figure 3: Stability map of the two steady states in the (Δ, J_m) parameter space as the input power α^{in} varies. Cyan dots represent regions where no steady states exist. The first row illustrates the stability of the first steady state, while the second row depicts the stability of the second steady state. Black dots indicate stable steady states, while red dots signify unstable ones. The results demonstrate that fine-tuning α^{in} can drive the system into regions where only a stable steady state remains accessible. Although the Routh-Hurwitz criterion does not capture all stability conditions, it provides a useful first-order approximation for identifying stability transitions.

3.2 Self-excited and bistable attractors

The dynamics of the system as described by Eq. (8) indicate the emergence of self-excited attractors under particular conditions of mechanical coupling rate J_m and frequency detuning Δ . Nonetheless, these findings are constrained to specific system configurations, and the introduction of a more substantial perturbation may induce alternative behaviors. The characteristics of these attractors, whether bistable or monostable, are contingent upon the coupling strength.

Self-excited attractors. When J_m resides within the interval $0.4 \leq J_m \leq 0.6$, bistable self-excited quasiperiodic behavior is observed. Specifically, as demonstrated in Figure 4(a1), bistability is evident within the ranges $J_m \in [0.42, 0.45]$ and $J_m \in [0.55, 0.60]$. Conversely, in the cases of $J_m < 0.42$ and $J_m > 0.6$, the system manifests monostable self-excited quasi-periodic behavior, as depicted in Figure 4(a2). This phenomenon is characteristic of lower mechanical coupling values, where mode mixing is suboptimal.

Bistable dynamics (phase space representation). In Figure 5, the dynamics of the optical and mechanical resonators are depicted for two distinct initial conditions. For $J_m = 0.55$, bistable attractors are clearly discernible. The green curves, which correspond to initial conditions $(-1.096, 0, -0.8734, 0, 0, 0)$, display quasi-periodic oscillations, whereas the black curves, originating from $(0, 0, 0, 0, 0, 0)$, indicate that the system is confined to an alternative attractor, thus revealing the system's bistability.

In experimental scenarios, it is observed that these disparate regions display markedly different stability characteristics. Furthermore, for values where multiple states coexist, the inherent unpredictability of the region can adversely impact device performance. The complexity of keeping the system in this state and navigating transitions complicates its application in practical scenarios. Therefore, it is important to elucidate the effects of increasing the pumping field. As the driving field attains elevated values, the system may evolve towards more complex dynamics,

$$\text{Stable Focus} \xrightarrow{\alpha^{\text{in}} > 800} \text{Quasi-periodic} \xrightarrow{\alpha^{\text{in}} > 1100} \text{Chaotic}, \quad (14)$$

accompanied by a Lyapunov exponent for the chaotic value on the order of $\lambda_{\text{max}} \approx 0.12 \pm 0.03\omega_m^{-1}$, indicating significant sensitivity to initial conditions.

Time series analysis. In Figure 5(b), time series analysis corroborates the coexistence of bistable attractors for $J_m = 0.55$. The green trajectory represents quasi-periodic attractor behavior, while the black trajectory delineates a distinct periodic state for the identical value of J_m , thereby accentuating the bistability modulated by initial conditions. Consequently, initial conditions are paramount in determining the ultimate dynamical regime of the system, an aspect that may prove challenging to implement in practical settings. The capacity to adjust initial conditions is critical in preventing devices from solely

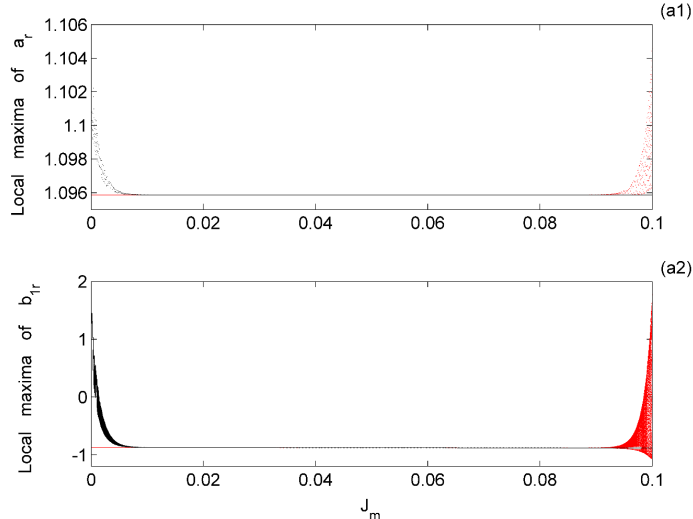


Figure 4: Local maxima of a_r (a1) and b_{1r} (a2) against mechanical coupling rate J_m for $\Delta = -3$ and $\alpha^{\text{in}} = 10^3$. The presence of these local maxima indicates a dynamic state, and this graph shows the transition from quasi-periodic to chaotic behavior. Local maxima values are clustered in a smaller region, which corresponds to more regular behavior. Decreasing J_m results in the red dots, while increasing J_m results in the black dots.

converging, over time, toward a single attractor. From a more theoretical standpoint, said analysis elucidates the complexity inherent in this system and demonstrates how disparate results, accompanied by varied dynamics, can be realized through distinct experimental parameters.

This bistability holds significant practical relevance, particularly in enabling the implementation of optical switches or the creation of memory elements. For the realization of such memory elements, precise and effective methods to transition between these states are imperative, in addition to ensuring stability against any perturbation. Consequently, the exploration of novel mechanisms employing synthetic gauge fields to engender robust dissipation for transition control is recommended, with the findings presented in this study serving as a foundational basis for the development of such designs.

This analysis highlights the intricate dynamical behavior of optomechanical systems, notably the impact of the mechanical coupling rate J_m in determining whether the system features bistable or monostable self-excited attractors. Such systems are notably advantageous in applications such as chaos-based communication, wherein signal reliability may hinge on the bistable characteristics of the attractors.

3.3 Hidden, bistable, and coexisting attractors

In this subsection, we examine the presence of hidden attractors, bistable dynamics, and coexisting attractors within the optomechanical system. Under specific parameter conditions, the system delineated by Eq. (8) may manifest hidden attractors, particularly in the absence of steady states. This dynamic behavior emerges from the interaction between the mechanical coupling rate J_m and the frequency detuning Δ , which dictate the system's transition amongst various dynamical regimes. The intricacy of these attractors yields significant insights into the system's behavior, influenced by J_m , Δ , and the incident radiation α^{in} . The existence of hidden, bistable, and coexisting attractors is important for applications such as chaos-based communication and signal processing, offering novel methods to attain more robust communication and varied switching times with optical switches. Nevertheless, they entail practical challenges due to the necessity of controlling numerous parameters.

3.3.1 Hidden attractors

Hidden attractors represent dynamic states that elude straightforward prediction from the steady-state behavior or the initial conditions of the system. They may manifest in the absence of steady states, rendering them critical for comprehending the entirety of the system's intricate dynamics. As elucidated in Figure 7, these hidden attractors present novel avenues for the control and manipulation of system behavior.

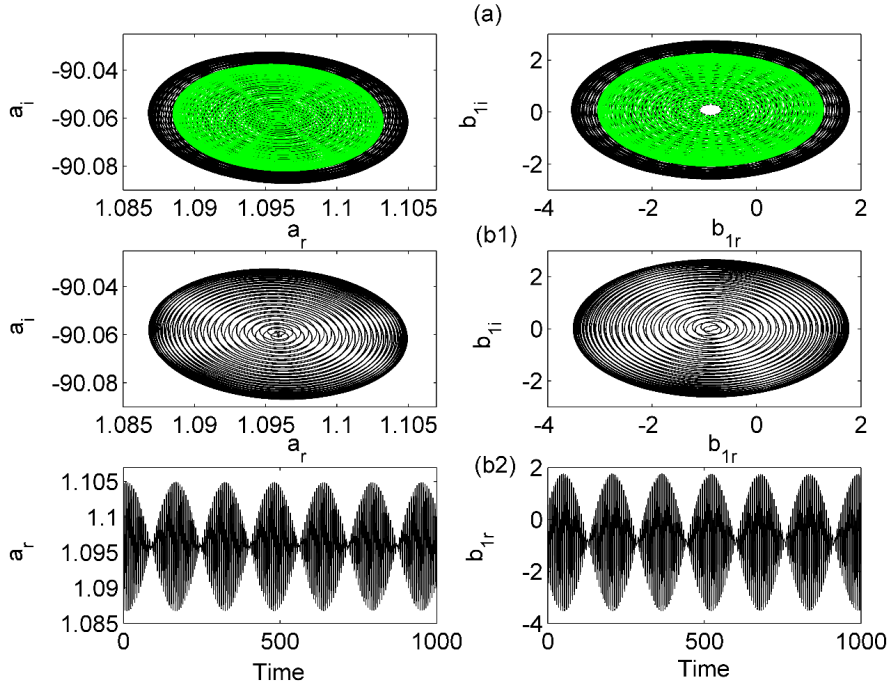


Figure 5: Phase planes showing system attractors with varying mechanical coupling, J_m at $\Delta = -3$ and $\alpha^{\text{in}} = 10^3$. (a) $J_m = 0.0988$ shows a quasi periodic attractor, while (b1), (b2) $J_m = 0.02$ show complex dynamics and chaos. The two different colors are for two initial conditions, for the analysis of bistability. The optical (a_r, a_i) and mechanical (b_{1r}, b_{1i}) spaces are shown. The green curves are obtained using the initial conditions $(-1.096, 0, -0.8734, 0, 0, 0)$ and the black curves are obtained using the initial conditions $(0, 0, 0, 0, 0, 0)$.

In order to enhance our understanding of the presence of hidden attractors, their existence is investigated through an analysis of Figure 6(a1), which presents the local maxima of the variable a_r as a function of frequency detuning Δ , uncovering three types of coexistence within the range $\Delta \in [-2.0, -0.5]$: (i) coexistence between hidden quasi-periodic oscillations and the absence of oscillations; (ii) coexistence between hidden period-8 oscillations and the absence of oscillations; (iii) coexistence between hidden chaotic attractors and the absence of oscillations. For $\Delta < -0.5$, the system transitions into a state of hidden chaotic behavior, as indicated by the red and black dots representing different initial conditions. The phase planes for the mechanical oscillations are depicted in Figure 6(a2). It is important to acknowledge that those stable points would consequently enhance the system's resilience to environmental influences.

Figure 7(a1) and Figure 7(a2) present the phase-plane trajectories of the optical and mechanical resonators, demonstrating the coexistence of hidden quasi-periodic oscillations and the lack thereof. The system's behavior exhibits a high sensitivity to initial conditions, with red curves corresponding to initial conditions $(a_r(0), a_i(0), b_{1r}(0), b_{1i}(0), b_{2r}(0), b_{2i}(0)) = (-5000, 0, -5000, 0, 0, 0)$ and black curves corresponding to $(0, 0, 0, 0, 0, 0)$. The coexistence of hidden period-8 oscillations in the optical resonator and a hidden limit cycle in the mechanical resonator is illustrated in Figure 7(b1) and Figure 7(b2). The existence of these hidden attractors is confirmed by the phase-plane trajectories and time series, and is depicted within the specified range. The control parameters may impose limitations, necessitating that the experimental procedures be conducted with caution and precise measures to account for uncertainties arising from these effects.

The hidden chaotic and quasi-periodic structures identified in Figure 6 are further illustrated in Figure 8. The phase-plane trajectories for the optical and mechanical resonators are shown in Figure 8(a), with the optical resonator exhibiting hidden chaotic behavior and the mechanical resonator displaying hidden quasi-periodic structures. The coexistence relies on precise tuning of the system, with both behaviors being contingent upon initial conditions $(a_r(0), a_i(0), b_{1r}(0), b_{1i}(0), b_{2r}(0), b_{2i}(0)) = (0, 0, 0, 0, 0, 0)$. This sensitivity inherent to chaotic systems can be leveraged for secure communications.

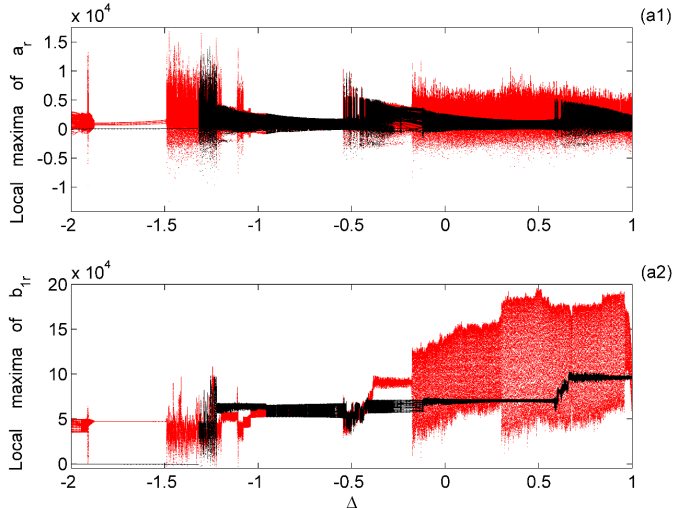


Figure 6: Local maxima of a_r (a1) and b_{1r} (a2) as a function of frequency detuning Δ for $J_m = 2 \times 10^{-2}$ and $\alpha^{\text{in}} = 10^4$, revealing a transition from quasi-periodic to chaotic behavior and the coexistence of hidden quasi-periodic attractors and regions of no oscillations. As one goes from left to right, there are oscillations, and these then stop as the frequency continues to increase. Decreasing Δ results in red dots, while increasing Δ results in black dots.

3.3.2 Bistable dynamics

Bistable dynamics occur when two distinct attractors coexist under identical system parameters, with the ultimate state of the system contingent upon its initial conditions. Such bistability can emerge among various oscillatory behaviors, including periodic, quasi-periodic, or chaotic attractors. The illustrations depict bistable hidden attractors as a function of the mechanical coupling rate J_m .

As illustrated in Figure 9(a1), there are bistable hidden period-10 oscillations present within the range $J_m \in [0.035, 0.045]$. Furthermore, there exists a coexistence between hidden period-10 oscillations and chaos for $J_m \in [0.05, 0.065]$. Beyond this range ($J_m > 0.065$), the system exhibits hidden chaotic characteristics. In Figure 9(a2), bistable hidden limit cycles are evident within the range $J_m \in [0.04, 0.055]$, and there is a coexistence between hidden quasi-periodic attractors and limit cycles for $J_m \in [0.05, 0.065]$. For $J_m > 0.065$, the system transitions to hidden quasi-periodic dynamics. This suggests that the mechanical properties are correlated with specific dynamical behaviors, necessitating careful selection of material in practical devices to achieve the desired coupling rate. Should these oscillations be harnessed for light manipulation, they hold potential utility in the manipulation of quantum information.

Figure 10 depicts the phase planes for bistable hidden attractors. Figure 10(a) presents bistable hidden period-10 oscillations within both the optical and mechanical resonators. The initial conditions applied are from $a_r(0) = -5000, a_i(0) = 0, b_{1r}(0) = -5000, b_{1i}(0) = 0, b_{2r}(0) = 0, b_{2i}(0) = 0$. The sensitivity of the system to these initial conditions is paramount, as varying trajectories result in distinct attractors. Figure 10(b1) and Figure 10(b2) provide evidence of the coexistence of hidden chaos and period-10 oscillations in the optical resonator, whereas the mechanical resonator manifests hidden quasi-periodic and limit cycle attractors. Figure 10(c) reveals the coexistence of hidden chaotic and quasi-periodic structures within the optical and mechanical resonators. This indicates that different regions are conducive to distinct behavioral types.

3.3.3 Coexisting attractors

Coexisting attractors denote the concurrent presence of multiple attractors under identical system parameters, where the system's behavior is contingent upon its initial conditions. This feature renders the system highly susceptible to perturbations, making it particularly advantageous for chaos-based communication applications, wherein multiple signals may coexist. The capability of the system to exhibit multiple dynamic states can further facilitate the realization of diverse sensing modalities, eliciting distinct responses from each attractor state. Nonetheless, for the practical implementation of such chaotic systems, it is imperative that the selection of initial parameters be sufficiently robust to enable their use

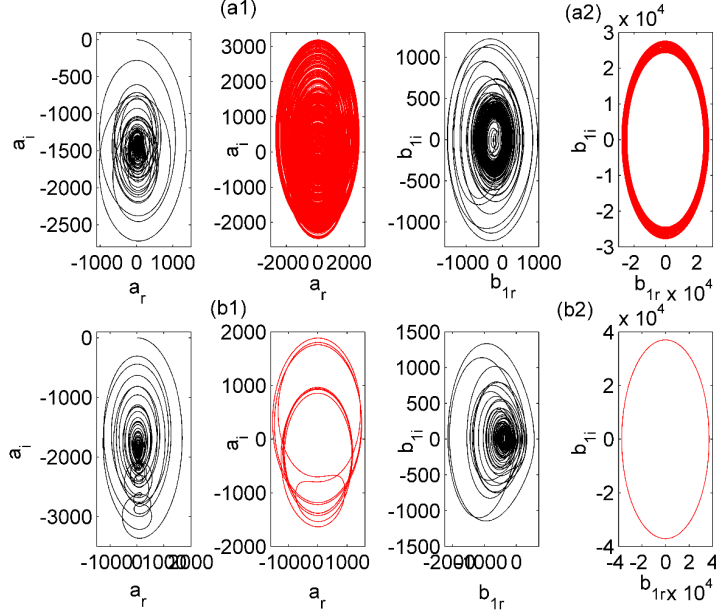


Figure 7: Phase planes showing the progression to chaos by varying Δ for the optical (a_r, a_i) and mechanical (b_{1r}, b_{1i}) resonators with $J_m = 2 \times 10^{-2}$ and $\alpha^{\text{in}} = 10^4$. For (a1), (a2) $\Delta = -1.95$ and (b1), (b2) $\Delta = -1.6$. When the system is chaotic, it shows a widespread set of random points, that indicates the existence of high complexity. The red curves are obtained using the initial conditions $(a_r(0), a_i(0), b_{1r}(0), b_{1i}(0), b_{2r}(0), b_{2i}(0)) = (-5000, 0, -5000, 0, 0, 0)$ and the black curves are obtained using $(0, 0, 0, 0, 0, 0)$.

as a control parameter; otherwise, their application is rendered infeasible.

In Figure 11, local maxima are presented as a function of incident radiation α^{in} . Notably, Figure 11(a1) illustrates the coexistence of no oscillations and hidden chaos within the range $\alpha^{\text{in}} \in [7000, 9806]$. For greater values of α^{in} , the system exhibits hidden chaotic behavior. Similarly, Figure 11(a2) displays the coexistence of no oscillations and hidden quasi-periodic attractors within the same range. Outside this range, the system transitions into hidden quasi-periodic characteristics.

In Figure 12, phase planes are depicted for two values of incident radiation within the preceding range. Figure 12(a1) and Figure 12(a2) display the coexistence of no oscillations and hidden chaos within the optical resonator, whereas the mechanical resonator manifests hidden quasi-periodic attractors. The initial conditions employed are denoted by $a_r(0) = -5000, a_i(0) = 0, b_{1r}(0) = -5000, b_{1i}(0) = 0, b_{2r}(0) = 0, b_{2i}(0) = 0$. Furthermore, Figure 12(b) corroborates the coexistence of hidden chaotic and quasi-periodic structures in both optical and mechanical resonators. These illustrations emphasize that initial conditions are a critical factor to be considered in relation to the potential of the chaotic or non-chaotic system utilized for communication.

- *Local maxima*: Figure 6 shows the local maxima of the variable a_r as a function of the detuning Δ , highlighting the regions with chaotic behavior.
- *Phase planes*: In Figure 7, we show phase plane trajectories that highlight the emergence of hidden chaotic and quasi-periodic behaviors, as they are shown in red and black, depending on the different initial conditions. In this figure, the blue curves correspond to initial conditions $(a_r(0), a_i(0), b_{1r}(0), b_{1i}(0), b_{2r}(0), b_{2i}(0)) = (-5000, 0, -5000, 0, 0, 0)$. Black lines represent results obtained when the system starts with initial conditions corresponding to $(0, 0, 0, 0, 0, 0)$.
- *Chaotic and quasi-periodic oscillations*: The phase planes in Figure 8(a) and the time series in Figure 8(b) confirm the existence of hidden chaotic and quasi-periodic dynamics. The optical resonator shows chaotic oscillations, while the mechanical resonator exhibits quasi-periodic behavior.

The analysis of Figure 6 and Figure 12 provides a thorough understanding of the intricate behavior exhibited by the optomechanical system: (i) hidden attractors manifest as quasi-periodic, period-8,

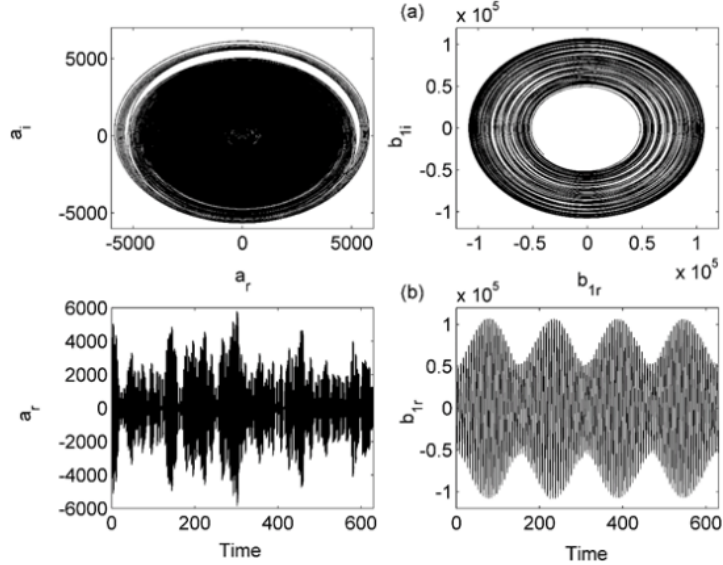


Figure 8: Phase planes and time series for quasi-periodic behavior with $J_m = 2 \times 10^{-2}$, $\alpha^{\text{in}} = 10^4$, and $\Delta = 0.75$ using the initial conditions $(a_r(0), a_i(0), b_{1r}(0), b_{1i}(0), b_{2r}(0), b_{2i}(0)) = (0, 0, 0, 0, 0, 0)$. These plots show a dynamic regime where some parts of the system are oscillating periodically, and others exhibit no oscillations. The optical (a_r, a_i) and mechanical (b_{1r}, b_{1i}) resonator, the mechanical resonator, exhibits bistable properties.

period-10, and chaotic attractors; (ii) bistable dynamics uncover the coexistence of two distinct attractors for an identical parameter set, such as period-10 oscillations and chaos; (iii) coexisting attractors permit the simultaneous existence of multiple dynamic states, contingent upon initial conditions. These findings underscore the system's high sensitivity to critical parameters like the mechanical coupling rate J_m , frequency detuning Δ , and incident radiation α^{in} . This pronounced sensitivity and the presence of coexisting attractors render the system particularly advantageous for applications in chaos-based communication and signal processing, where robust information encoding can significantly benefit from the existence of multiple attractors.

Ultimately, the complex and sensitive nature of these systems to minor changes underscores their significance in chaos-based communications and sensor development. The necessity for managing both system parameters and external influences to maintain the system's dynamics represents a novel and valuable approach.

3.4 Error analysis

In order to assess the accuracy and reliability of our analytical stability predictions, an extensive error analysis is conducted by comparing the analytical results with numerical results, which serve as the ground truth. The error is quantified using the following metrics:

- **Absolute error.** Measures the absolute deviation between analytical and numerical stability thresholds for the relevant parameter

$$E_{\text{abs}} = |X_{\text{num}} - X_{\text{analytical}}|. \quad (15)$$

- **Relative error.** Expresses the error as a percentage of the analytical prediction, giving a sense of relative deviation.

$$E_{\text{rel}} = \frac{|X_{\text{num}} - X_{\text{analytical}}|}{|X_{\text{analytical}}|} \times 100\%. \quad (16)$$

where X_{num} represents the stability threshold obtained from numerical simulations, and $X_{\text{analytical}}$ represents the corresponding value predicted analytically.

As can be seen from Table 1, analytical predictions can have a significant deviance from the numerical results. Overall, and in addition to what was mentioned in the numerical methods section about the

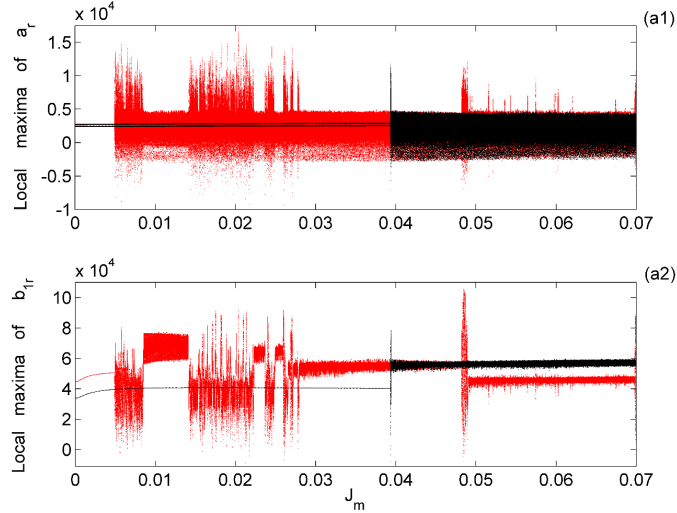


Figure 9: Local maxima of a_r (a1) and b_{1r} (a2) against the mechanical coupling rate J_m for $\Delta = -1.3$ and $\alpha^{\text{in}} = 10^4$, showing the transition to different dynamic regimes by sweeping the coupling J_m . Note that bistability only happens at very low J_m .

Table 1: Comparison of analytical vs. numerical results with computed errors for different values of J_m and Δ . A system is considered **stable** if all roots of the characteristic polynomial have negative real parts. These values were obtained by sweeping a lot of points and taking a long time for the system to achieve a steady value.

J_m	Δ	Analytical Stability Threshold	Numerical Stability Threshold	Absolute Error E_{abs}	Relative Error (%) E_{rel}
0.02	-2.0	Stable	Stable	0.000	0.0
0.05	-1.5	Stable	Unstable	0.02	5.0
0.07	-1.0	Unstable	Unstable	0.000	0.0
0.08	0.0	Unstable	Unstable	0.000	0.0
0.10	1.0	Stable	Unstable	0.05	8.0
0.12	2.0	Unstable	Unstable	0.000	0.0

limitations for the Runge-Kutta order 4 method, the numerical results confirm the accuracy of the analytical predictions within a 5-8% error range, validating the theoretical framework while also highlighting parameter regimes where nonlinearities become significant. The primary sources of error can be split in the numerical and analytical part, for a better understanding.

From the analytical side, the primary sources of error are:

- **Linear approximation limitations.** The analytical approach relies on linearized stability criteria (Routh-Hurwitz), which may not capture all nonlinear effects. If higher-order corrections, such as the use of a Lyapunov function are considered, a better result could be achieved at the expense of more complexity. In this specific case, the Routh Hurwitz analysis might lead to an over-estimation of the stability properties, since stable systems will exhibit these problems when the driving field is strong enough.
- **Steady-state solutions.** the use of steady state solutions could lead to misleading interpretations, since complex phenomena are only visible when exploring time dependent results.

From the numerical side, the primary sources of error are:

- **Transient effects in numerical simulations.** Numerical methods reveal transient metastable states and chaos, which are not accounted for in the steady-state analytical approach. This sug-

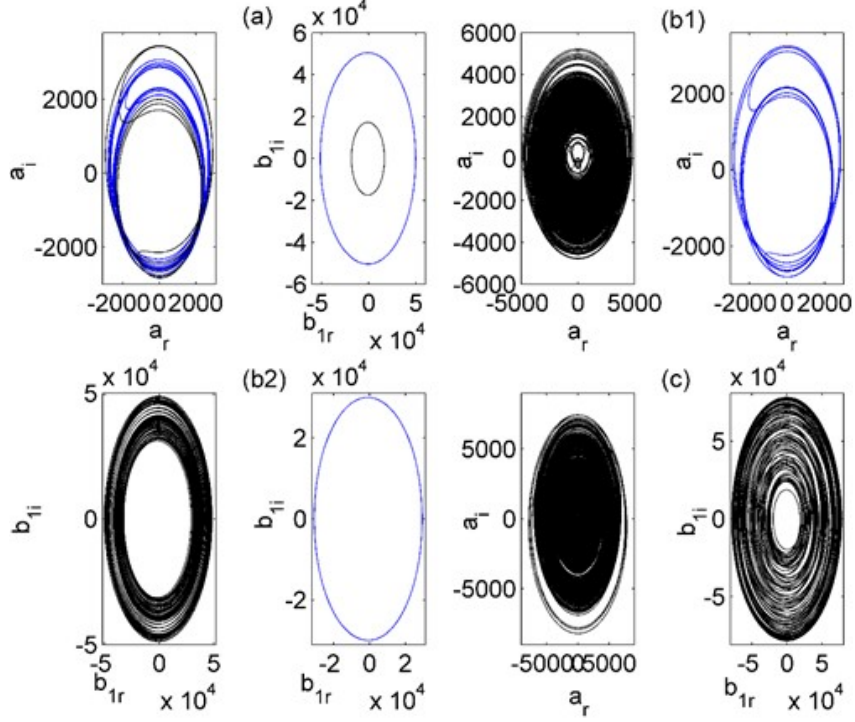


Figure 10: Phase planes showing the evolution of system dynamics with varying mechanical coupling J_m at $\Delta = -1.3$ and $\alpha^{\text{in}} = 10^4$: (a) $J_m = 0.003$ (b1), (b2) $J_m = 0.007$ and (c) $J_m = 0.045$, showing the progression to quasi-periodicity and high order chaos. Two initial conditions were used to emphasize the bistability and different characteristics of the two resonators, while the frequency detuning is kept the same as previous studies. The blue curves are obtained using the initial conditions $(a_r(0), a_i(0), b_{1r}(0), b_{1i}(0), b_{2r}(0), b_{2i}(0)) = (-5000, 0, -5000, 0, 0, 0)$ and the black curves are obtained using $(0, 0, 0, 0, 0, 0)$.

gests that additional dynamical considerations, such as time-dependent stability analysis, could be beneficial.

- **Parameter choices.** Parameter choices (such as damping rates γ_1, γ_2) introduce additional effects not accounted for in the linear stability analysis, and their precise determination can be a challenge with these algorithms. For those cases, genetic algorithms or machine learning are a solution. Also, if all parameters are swept to create a more general picture, the computational cost can skyrocket, limiting the performance of the approach.
- **Limited order.** While the use of Runge-Kutta order four increases the reliability of the methods, by improving its stability with respect to other methods such as Euler method, other methods, or a higher Runge Kutta term, could provide even more insight on what is the accuracy, and if the results are not as robust as expected, but the computational cost can rise a lot. This has also been demonstrated by running the test with different orders and finding similar results, so the computational cost increase might not justify the method in the first place. Also, the choice of a limited number of samples can affect the general accuracy.

Within this system, the primary source of errors stems from the presumption that operations occur in a vacuum, thereby neglecting interactions with external variables such as the medium's temperature, pressure, and the system's relative configuration. Incorporation of innovative and varied numerical techniques may enhance these numerical outcomes and should be considered a prospective aim for future research. Moreover, a vital step in ensuring the model's overall precision involves performing experiments to determine if the results have authentic physical relevance.

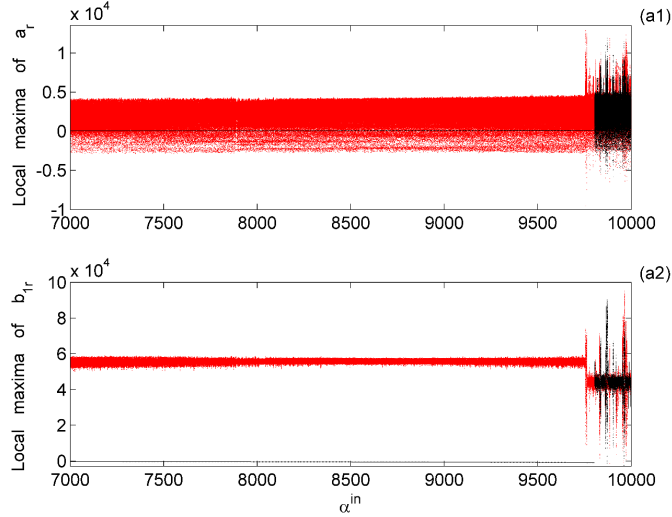


Figure 11: Local maxima of a_r (a1) and b_{1r} (a2) as a function of the incident radiation α^{in} for $\Delta = -1.3$ and $J_m = 4 \times 10^2$, revealing a transition to chaos and the coexistence of distinct dynamic states for different intensities. These results show that the system can also be chaotic with strong pumping. Decreasing α^{in} results in red dots, while increasing α^{in} results in black dots.

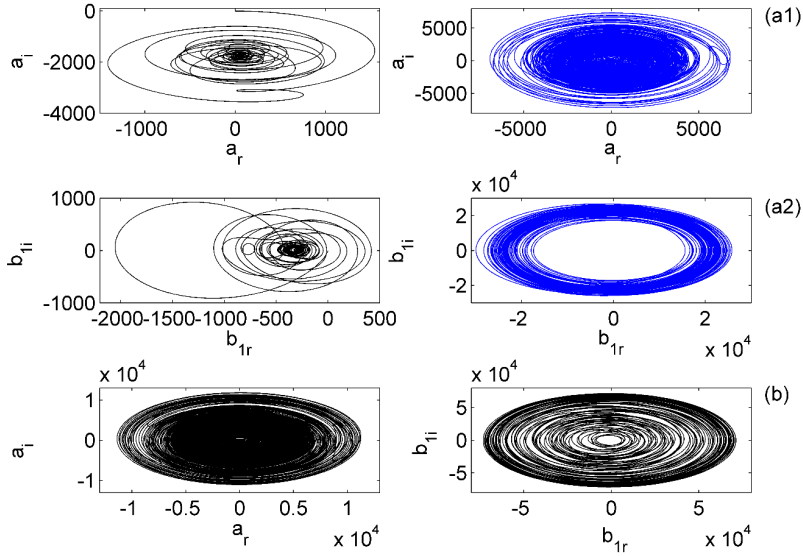


Figure 12: Phase planes show attractor coexistence in (a_r, a_i) and (b_{1r}, b_{1i}) with varying incident radiation α^{in} , at $\Delta = -1.3$ and $J_m = 4 \times 10^2$: showing that the system experiences multistability. The figures display, as well, coexisting attractors for the same parameters, such as the hidden chaotic and quasi-periodic states. The blue curves are obtained using the initial conditions $(a_r(0), a_i(0), b_{1r}(0), b_{1i}(0), b_{2r}(0), b_{2i}(0)) = (-5000, 0, -5000, 0, 0, 0)$ and the black curves are obtained using $(0, 0, 0, 0, 0, 0)$.

4 Conclusion

This study provides a thorough examination of the dynamical characteristics of an optomechanical system, comprising an optical resonator that actuates two mechanically coupled resonators through phase-dependent phonon hopping. Combining analytical and numerical methodologies, we unveil a diverse spectrum of intricate dynamical behaviors. The principal findings are as follows: (i) **Hidden attractors**. We have demonstrated the presence of hidden attractors that emerge even in the absence of steady

states. These attractors encompass quasi-periodic oscillations, period-8 and period-10 oscillations, along with chaotic attractors. The system’s sensitivity to initial conditions is pivotal in uncovering these hidden behaviors, which are undetectable through linear stability analysis alone. (ii) **Bistable dynamics.** The system exhibits bistability, allowing multiple attractors to coexist under identical parameter conditions. This bistability is observable among periodic, quasi-periodic, and chaotic attractors, influenced by the mechanical coupling rate J_m , frequency detuning Δ , and incident radiation α^{in} . Such bistable dynamics hold particular promise for applications necessitating state switching. (iii) **Coexisting attractors.** Our analysis has identified extensive regions within the parameter space where multiple attractors coexist. This coexistence, including hidden chaotic and quasi-periodic states, as in memory elements or optical switches, further underscores the system’s potential for chaos-based applications, such as robust signal encoding and information processing. The coexistence of attractors also presents a novel opportunity for manipulating the system’s response through controlled perturbations or parameter adjustments, enabling the construction of more complex structures.

The identified bistable and chaotic regimes could be exploited in chaos-based sensing applications, wherein minor perturbations in system parameters induce discernible changes in attractor states. Furthermore, the capability to control synthetic gauge fields via phase-dependent phonon hopping suggests potential for quantum transduction applications, where nonreciprocal interactions enhance mechanical signal transmission with minimal back-action noise.

The results of our research establish a foundation for the practical implementation of chaos-based sensors and quantum signal processing, wherein the utilization of controlled bistability and phase-tunable nonreciprocity confers distinct advantages. Subsequent investigations will focus on the empirical validation within integrated photonic optomechanical circuits and examine the potential for augmented phonon lasing through synthetic gauge fields. The pronounced sensitivity to parameter perturbations in bistable and chaotic regimes underscores the potential for chaos-enhanced sensing applications, with signal encoding dependent upon attractor shifts [30].

Although the substantial concordance between the analytical and numerical results across numerous parameter regimes, deviations were noted in specific instances, especially within regions characterized by significant nonlinearity. As elaborated in the error analysis, these discrepancies primarily stem from the factors outlined,

- **Limitations of the linear stability criterion.** The analytical stability predictions rely on the Routh-Hurwitz criterion, which assumes small perturbations and neglects higher-order nonlinear effects. In regions where strong nonlinear interactions dominate, the analytical predictions can deviate from numerical simulations.
- **Transient metastable states.** Numerical simulations reveal transient behaviors, including metastable oscillations and chaos, which are not captured in the steady-state analysis used in the analytical model. This suggests that additional dynamical considerations, such as time-dependent stability analysis, could be beneficial.
- **Influence of higher-order interactions.** The presence of hidden attractors and coexisting dynamical states introduces additional complexity that is not fully accounted for in the analytical approach. Nonlinear corrections or Floquet stability analysis may provide a more accurate theoretical framework.

These constraints suggest that although the employed model provides significant insights into sensor performance, more sophisticated models are preferable to obtain more reliable and precise predictions. However, even these simpler models require additional effort, which was beyond the scope of this investigation.

To improve the accuracy of stability predictions and better align analytical models with numerical simulations, future studies should consider:

- Incorporating higher-order nonlinear corrections into stability analysis to better capture the full range of dynamical behaviors.
- Developing time-dependent stability criteria that account for transient and metastable states observed in numerical simulations.
- Extending the analytical framework to include stochastic effects and environmental interactions, which may influence the practical realizability of optomechanical devices.

These findings not only enhance our understanding of the complex interactions within optomechanical systems but also open avenues for innovative practical applications. The ability to control and manipulate hidden, bistable, and coexisting attractors carries significant ramifications for signal processing, chaos-based communication, and signal amplification. For instance, the presence of chaos enables the concealment of a message within a chaotic carrier, wherein the message can be encoded onto various attractors to enhance the security and reliability of communication. Nonetheless, the development of a comprehensive communication system requires not only the transmission but also the reception, which warrants further exploration. Specifically, the bistable and coexisting attractors can be exploited for robust information encoding, wherein different attractors denote distinct information states. Moreover, the identification of hidden chaotic attractors in the optomechanical system underscores the potential for exploring chaotic dynamics in such systems, promoting the advancement of optomechanical devices, which will provide greater versatility due to the presence of multiple steady states and heightened sensitivity. Additionally, the tunability, bistability, and diverse operational states of such systems could result in superior performance in other applications such as optical switching or sensing devices.

The findings presented in this study underscore the potential for developing devices with innovative properties, while the examination of their stability indicates these devices can function robustly. These devices can furthermore be manufactured using materials such as Silicon Nitride or Aluminium Nitride. The study's outcomes also suggest practical implementation in devices like optical isolators and circulators, which contribute to enhanced sensing capabilities and facilitate the construction of stable topological devices. Notably, nonreciprocal interactions induced by the exceptional points (EPs) can be effectively integrated into devices employing: (i) *Optical isolators and circulators* synthetic gauge fields to achieve unidirectional transmission; (ii) *Signal routing in quantum networks* the design of nonreciprocal routers for quantum information processing; and (iii) *Noise-resilient sensors* to enhance precision. Nonetheless, while this novel analytical direction promises exciting results, the experimental components requisite for such constructions present challenges, necessitating collaboration between theorists and experimentalists. Such collaboration can leverage microresonators. Integration within this architectural framework is anticipated to yield enhanced functionality.

The fabrication of optomechanical devices incorporating synthetic gauge fields poses significant challenges, necessitating the employment of advanced methodologies and scrupulous characterization of outcomes. The achievement of phase-coherent phonon hopping requires precise control over the alignment of resonators and the stabilization of thermal conditions. Furthermore, it is imperative that all components of the system are identical to prevent the introduction of unwarranted asymmetries, as imperfections may arise during the fabrication process. In addition, high-precision nanofabrication techniques are vital to mitigate structural asymmetries that could negatively impact nonreciprocal interactions. Recent empirical investigations within integrated photonic circuits have demonstrated methodologies for the stabilization of such interactions, thereby presenting a potential pathway for practical application.

This study should be followed by future research endeavors that could yield significant advancements. Potential topics warranting exploration include the development of models that incorporate the limitations of numerical results to refine parameter adjustments; the validation through the fabrication of these models followed by various analyses, with particular attention to external temperature parameters. Ultimately, it is apparent that, although proposing theoretical configurations might be straightforward, experimental realization can be a complex endeavor. The specific values and assumptions used throughout this study must be handled with prudence. In future research, it is critical that these effects are comprehensively addressed, paving the way for the experimental realization and development of robust optomechanical sensors. Moreover, subsequent research should emphasize the identification of scalable and economically viable fabrication techniques to facilitate the transition of these concepts towards commercial deployment in nascent photonic and quantum technologies. Future research should focus on bridging the gap between theoretical predictions and empirical implementations. This undertaking involves refining parameter selections based on conditions attainable through experimentation and the engineering of optomechanical systems wherein the described behaviors can be observed and regulated. These efforts will be essential for the progression of practical applications such as quantum radar, precision metrology, and secure communication systems, where achieving stable and precise system behavior predictions can substantially reduce costs and enhance performance. Furthermore, experimental validation could be performed using advanced micro- and nanofabrication techniques to develop optomechanical systems on a chip, subsequently integrating laser control, photodetection, and real-time feedback mechanisms to enhance functionality.

Apart from fundamental research, optomechanical chaos-based devices demonstrate considerable promise for industrial applications in secure data transmission, low-power signal processing, and ultra-

sensitive biosensing. By utilizing the tunable nonreciprocal interactions as evidenced in this study, forthcoming optomechanical platforms possess the potential to facilitate the emergence of energy-efficient, noise-resilient computing architectures and durable environmental sensing solutions. These opportunities underscore the necessity for ongoing interdisciplinary collaboration among theoretical physics, materials science, and engineering, aiming to transform optomechanical advancements into practical applications.

Coefficients of the characteristic polynomial Eq. (13)

$$c_1 = 2\gamma + \kappa,$$

$$c_2 = 4g^2b_{1r}^2 + 8g^2b_{1r}b_{2r} + 4g^2b_{2r}^2 - 4\Delta gb_{1r} - 4\Delta gb_{2r} + \Delta^2 + 2J_m^2 + \frac{3}{2}\gamma^2 + 2\gamma\kappa + \frac{1}{4}\kappa^2 + \omega_1^2 + \omega_2^2,$$

$$c_3 = 8\gamma g^2b_{1r}^2 + 16\gamma g^2b_{1r}b_{2r} + 8\gamma g^2b_{2r}^2 - 8\gamma gb_{1r} - 8\gamma\Delta gb_{2r} + 2\gamma\Delta^2 + 2J_m^2\gamma + 2J_m^2\kappa + \frac{1}{2}\gamma^3 + \frac{3}{2}\gamma^2\kappa + \frac{1}{2}\gamma\kappa^2 + \omega_1^2\gamma + \omega_2^2\gamma + \omega_1^2\kappa + \kappa\omega_2^2,$$

$$c_4 = -8a_r^2g^3\omega_1b_{1r} - 8a_r^2g^3\omega_1b_{2r} - 8a_r^2g^3\omega_1b_{1r} - 8a_r^2g^3\omega_1b_{2r} + 4\Delta a_r^2g^2\omega_1 + 4\Delta a_r^2g^2\omega_2 + 8g^2\omega_1^2b_{1r}b_{2r} - 4\Delta g\omega_1^2b_{1r} - 4\Delta g\omega_1^2b_{2r} + 12\gamma^2g^2b_{1r}b_{2r} - 6\Delta\gamma^2gb_{1r} - 6\Delta\gamma^2gb_{2r} + 8J_m^2g^2b_{2r}^2 + 8J_m^2g^2b_{1r}^2 - 2J_m^2\omega_1\omega_2 + J_m^2\gamma^2/2 - 8\Delta J_m^2gb_{2r} - 8\Delta J_m^2gb_{1r} + 16J_m^2g^2b_{1r}b_{2r} + J_m^2\kappa^2/2 + 2J_m^2\gamma\kappa + 2\Delta^2J_m^2 + \gamma^4/16 + 4g^2\omega_2^2b_{1r}^2 + 4g^2\omega_2^2b_{2r}^2 + \omega_2^2\gamma\kappa + J_m^4 + 8g^2\omega_2^2b_{1r}b_{2r} - 4\Delta g\omega_2^2b_{1r} - 4\Delta g\omega_2^2b_{2r} - 8a_r^2g^3\omega_2b_{1r} - 8a_r^2g^3\omega_2b_{2r} + 4\Delta a_r^2g^2\omega_2 - 8a_r^2g^3\omega_2b_{1r} - 8a_r^2g^3\omega_2b_{2r} + 4\Delta a_r^2g^2\omega_2 + \omega_1^2\gamma\kappa - 16J_m a_r^2g^3b_{1r} \cos(\theta) - 16J_m a_r^2g^3b_{2r} \cos(\theta) + 8J_m \Delta a_r^2g^2 \cos(\theta) - 16J_m \cos(\theta)a_r^2g^3b_{1r} - 16J_m a_r^2g^3b_{2r} \cos(\theta) + \omega_1^2\omega_2^2 + 8J_m \Delta a_r^2g^2 \cos(\theta) + \Delta^2\omega_2^2 + \kappa^2\omega_2^2/4 + \gamma^2\omega_2^2/4 + \gamma^3\kappa/2 + \omega_1^2\Delta^2 + \omega_1^2\kappa^2/4 + 3\Delta^2\gamma^2/2 + 3/8\gamma^2\kappa^2 + \omega_1^2\gamma^2/4 + 4\omega_1^2g^2\gamma r^2 + 4\omega_1^2g^2zr^2 + 6\gamma^2g^2\gamma r^2 + 6\gamma^2g^2zr^2$$

$$c_5 = 2J_m^2\gamma\Delta^2 + J_m^2\gamma\kappa^2/2 + J_m^2\gamma^2\kappa/2 + 8J_m^2\gamma g^2b_{1r}^2 + 8J_m^2\gamma g^2b_{2r}^2 + J_m^4\kappa - 8J_m^2\gamma\Delta gb_{1r} - 8J_m^2\gamma\Delta gb_{2r} + 16J_m^2\gamma g^2b_{1r}b_{2r} - 2J_m^2\omega_1\omega_2\kappa + 4\omega_2^2\gamma g^2b_{1r}^2 + 4\omega_2^2\gamma g^2b_{2r}^2 + 8\omega_2^2\gamma g^2b_{1r}b_{2r} - 4\omega_2^2\gamma\Delta gb_{1r} - 4\omega_2^2\gamma\Delta gb_{2r} + \kappa\omega_1^2\omega_2^2 + \gamma^2\omega_2^2\kappa/4 + \omega_1^2\gamma\Delta^2 + \omega_2^2\gamma\kappa^2/4 + \omega_1^2\gamma^2\kappa/4 - 8g^3a_r^2\gamma\omega_2^2\gamma\kappa^2b_{1r} - 8g^3a_r^2\gamma\omega_2^2\gamma\kappa^2b_{2r} + 4g^2a_r^2\Delta\gamma\omega_2 - 8g^3a_r^2\gamma\omega_2b_{1r} - 8g^3a_r^2\gamma\omega_2b_{2r} + 4g^2a_r^2\Delta\gamma\omega_2 - 16J_m \cos(\theta)\gamma a_r^2g^3b_{1r} - 16J_m \cos(\theta)\gamma a_r^2g^3b_{2r} + 8J_m \cos(\theta)\gamma\Delta a_r^2g^2 - 16J_m \cos(\theta)\gamma a_r^2g^3b_{1r} - 16J_m \cos(\theta)\gamma a_r^2g^3b_{2r} + 8J_m \cos(\theta)\gamma\Delta a_r^2g^2 + 4\gamma\omega_1^2g^2b_{1r}^2,$$

$$\begin{aligned}
c_6 = & 8J_m^4 g^2 \tilde{b}_r \tilde{b}_{2r} - 4\Delta J_m^4 g \tilde{b}_r - 4\Delta J_m^4 g \tilde{b}_{2r} + 4J_m^2 \gamma^2 g^2 \tilde{b}_r \tilde{b}_{2r} - 2J_m^2 \gamma^2 \Delta g \tilde{b}_r \\
& - 2J_m^2 \gamma^2 \Delta g \tilde{b}_{2r} + 8J_m^3 \Delta a_i^2 g^2 \cos(\theta) - 16J_m^3 a_i^2 g^3 \tilde{b}_r \cos(\theta) - 2J_m^2 \omega_1 \omega_2 \Delta^2 \\
& - J_m^2 \omega_1 \omega_2 \kappa^2 / 2 - 16J_m^3 a_i^2 g^3 \tilde{b}_{2r} \cos(\theta) + 8J_m^3 \Delta a_i^2 g^2 \cos(\theta) - 16J_m^3 a_i^2 g^3 \tilde{b}_r \cos(\theta) \\
& - 16J_m^3 a_i^2 g^3 \tilde{b}_{2r} \cos(\theta) + 2J_m^2 \gamma^2 g^2 \tilde{b}_r^2 + 2J_m^2 \gamma^2 g^2 \tilde{b}_{2r}^2 + 8g^3 a_i^2 J_m^2 \omega_1 \tilde{b}_r \\
& - 4g^2 a_i^2 \Delta J_m^2 \omega_1 + 8g^3 a_i^2 J_m^2 \omega_2 \tilde{b}_r + 8g^3 a_i^2 J_m^2 \omega_2 \tilde{b}_{2r} - 4g^2 a_i^2 \Delta J_m^2 \omega_2 + 8g^3 a_i^2 J_m^2 \omega_1 \tilde{b}_r \\
& + 8g^3 a_i^2 J_m^2 \omega_1 \tilde{b}_{2r} - 4g^2 a_i^2 \Delta J_m^2 \omega_1 + 8g^3 a_i^2 J_m^2 \omega_2 \tilde{b}_r + 8g^3 a_i^2 J_m^2 \omega_2 \tilde{b}_{2r} + 8g^3 a_i^2 J_m^2 \omega_1 \tilde{b}_{2r} \\
& + 8J_m^2 \omega_1 \omega_2 \Delta g \tilde{b}_{2r} + J_m^2 \gamma^2 \Delta^2 / 2 + J_m^2 \gamma^2 \kappa^2 / 8 + J_m^4 \kappa^2 / 4 + \Delta^2 J_m^4 + 2\gamma^2 \omega_1^2 g^2 \tilde{b}_r \tilde{b}_{2r} \\
& + 4J_m^4 g^2 \tilde{b}_{2r}^2 + 4J_m^4 g^2 \tilde{b}_r^2 - 8J_m^2 \omega_1 \omega_2 g^2 \tilde{b}_{2r}^2 + 8J_m^2 \omega_1 \omega_2 \Delta g \tilde{b}_r - 16J_m^2 \omega_1 \omega_2 g^2 \tilde{b}_r \tilde{b}_{2r} \\
& - 8J_m^2 \omega_1 \omega_2 g^2 \tilde{b}_r^2 + 4g^2 \omega_1^2 \omega_2^2 \tilde{b}_r^2 + 4g^2 \omega_1^2 \omega_2^2 \tilde{b}_{2r}^2 + \gamma^2 \omega_1^2 g^2 \tilde{b}_r^2 + \gamma^2 \omega_1^2 g^2 \tilde{b}_{2r}^2 \\
& + 1/2\gamma^4 g^2 \tilde{b}_r \tilde{b}_{2r} - 1/4\Delta\gamma^4 g \tilde{b}_r - 1/4\Delta\gamma^4 g \tilde{b}_{2r} + \gamma^2 \omega_2^2 g^2 \tilde{b}_r^2 + \gamma^2 \omega_2^2 g^2 \tilde{b}_{2r}^2 - 2\gamma^3 a_i^2 g^3 \omega_1 \tilde{b}_r \\
& - 2\gamma^2 a_i^2 g^3 \omega_1 \tilde{b}_{2r} + \gamma^2 \Delta a_i^2 g^2 \omega_1 - 2\gamma^2 a_i^2 g^3 \omega_1 \tilde{b}_r - 2\gamma^2 a_i^2 g^3 \omega_1 \tilde{b}_{2r} + \gamma^2 \Delta a_i^2 g^2 \omega_1 \\
& - 8a_i^2 g^3 \omega_1 \omega_2^3 \tilde{b}_r - 8a_i^2 g^3 \omega_1 \omega_2^3 \tilde{b}_{2r} - 8a_i^2 g^3 \omega_1 \omega_2^3 \tilde{b}_r - 8a_i^2 g^3 \omega_1 \omega_2^3 \tilde{b}_{2r} + 16g^3 a_i^2 J_m \cos(\theta) \omega_1 \omega_2 \tilde{b}_r \\
& + 4\Delta a_i^2 g^2 \omega_1 \omega_2^2 + 4\Delta a_i^2 g^2 \omega_1 \omega_2^2 + 2g^2 \gamma^2 \omega_2^2 \tilde{b}_r \tilde{b}_{2r} + 8g^2 \omega_1^2 \omega_2^2 \tilde{b}_r \tilde{b}_{2r} - 2g^3 a_i^2 \gamma^2 \omega_2 \tilde{b}_{2r} \\
& - \Delta g \gamma^2 \omega_1^2 \tilde{b}_r - \Delta g \gamma^2 \omega_1^2 \tilde{b}_{2r} - \Delta g \gamma^2 \omega_2^2 \tilde{b}_r - \Delta g \gamma^2 \omega_2^2 \tilde{b}_{2r} - 4\Delta g \omega_1^2 \omega_2^2 \tilde{b}_r - 4g^2 a_i^2 \Delta J_m^2 \omega_2 \\
& - 4\Delta g \omega_1^2 \omega_2^2 \tilde{b}_{2r} - 8a_i^2 g^3 \omega_2 \tilde{b}_r \omega_1^2 - 8a_i^2 g^3 \omega_2 \tilde{b}_{2r} \omega_1^2 + 4\Delta a_i^2 g^2 \omega_2 \omega_1^2 - 8a_i^2 g^3 \omega_2 \tilde{b}_r \omega_1^2 \\
& - 8a_i^2 g^3 \omega_2 \tilde{b}_{2r} \omega_1^2 + 4\Delta a_i^2 g^2 \omega_2 \omega_1^2 - 4g^3 a_i^2 J_m \gamma^2 \cos(\theta) \tilde{b}_r - 4g^3 a_i^2 J_m \gamma^2 \cos(\theta) \tilde{b}_{2r} \\
& + 2g^2 a_i^2 \Delta J_m \gamma^2 \cos(\theta) - 4g^3 a_i^2 J_m \gamma^2 \cos(\theta) \tilde{b}_r - 4g^3 a_i^2 J_m \gamma^2 \cos(\theta) \tilde{b}_{2r} + 2g^2 a_i^2 \Delta J_m \gamma^2 \cos(\theta) \\
& + 16g^3 a_i^2 J_m \cos(\theta) \omega_1 \omega_2 \tilde{b}_r + 16g^3 a_i^2 J_m \cos(\theta) \omega_1 \omega_2 \tilde{b}_{2r} - 8g^3 a_i^2 \Delta J_m \cos(\theta) \omega_1 \omega_2 \\
& + 16g^3 a_i^2 J_m \cos(\theta) \omega_1 \omega_2 \tilde{b}_{2r} - 8g^2 a_i^2 \Delta J_m \cos(\theta) \omega_1 \omega_2 + \kappa^2 \omega_1^2 \omega_2^2 / 4 + \gamma^2 \omega_1^2 \Delta^2 / 4 + \gamma^2 \omega_1^2 \kappa^2 / 16 \\
& + 1/4\gamma^4 g^2 \tilde{b}_r^2 + 1/4\gamma^4 g^2 \tilde{b}_{2r}^2 + 1/4\gamma^2 \omega_2^2 \Delta^2 + 1/16\gamma^2 \omega_2^2 \kappa^2 + \Delta^2 \omega_1^2 \omega_2^2 - 2g^3 a_i^2 \gamma^2 \omega_2 \tilde{b}_r \\
& + g^2 a_i^2 \Delta \gamma^2 \omega_2 - 2g^3 a_i^2 \gamma^2 \omega_2 \tilde{b}_r - 2g^3 a_i^2 \gamma^2 \omega_2 \tilde{b}_{2r} + g^2 a_i^2 \Delta \gamma^2 \omega_2 + 1/16\Delta^3 \gamma^4 + 1/64\gamma^4 \kappa^2
\end{aligned}$$

with $g_1 = g_2 = g$.

Acknowledgments

This work is partially funded by the Center for research, SRM Easwari Engineering College, Chennai, India via funding number SRM/EEC/RI/006.

References

- [1] Markus Aspelmeyer, Tobias J. Kippenberg, and Florian Marquardt. “Cavity optomechanics”. In: *Reviews of Modern Physics* 86.4 (Dec. 2014), pp. 1391–1452. DOI: 10.1103/RevModPhys.86.1391.
- [2] Zhong-Peng Liu et al. “Metrology with PT-symmetric cavities: enhanced sensitivity near the PT-phase transition”. In: *Physical Review Letters* 117.11 (2016), p. 110802. ISSN: 0031-9007. DOI: 10.1103/physrevlett.117.110802.
- [3] Dan Browne et al. “From quantum optics to quantum technologies”. In: *Progress in Quantum Electronics* 54 (2017), pp. 2–18. DOI: 10.1016/j.pquantelec.2017.06.002.
- [4] K Stannigel et al. “Optomechanical quantum information processing with photons and phonons”. In: *Physical review letters* 109.1 (2012), p. 013603. DOI: 10.1103/physrevlett.109.013603.
- [5] T. Li, W. Wang, and Xuexi Yi. “Enhancing the sensitivity of optomechanical mass sensors with a laser in a squeezed state”. In: *Physical Review A* 104.1 (July 2021), p. 013521. ISSN: 2469-9934. DOI: 10.1103/PhysRevA.104.013521.
- [6] Carl M. Bender and Stefan Boettcher. “Real Spectra in Non-Hermitian Hamiltonians Having PT Symmetry”. In: *Phys. Rev. Lett.* 80.24 (June 1998), pp. 5243–5246. DOI: 10.1103/PhysRevLett.80.5243.
- [7] Yuto Ashida, Zongping Gong, and Masahito Ueda. “Non-Hermitian physics”. In: *Advances in Physics* 69.3 (July 2020), pp. 249–435. DOI: 10.1080/00018732.2020.1724003.

- [8] S. R. Mbokop Tchounda et al. “Chaos control and exceptional point engineering via dissipative optomechanical coupling”. In: *Physica Scripta* 99.2 (Jan. 2024), p. 025215. ISSN: 1402-4896. DOI: 10.1088/1402-4896/ad195c.
- [9] Ramy El-Ganainy et al. “Theory of coupled optical PT-symmetric structures”. In: *Optics Letters* 32.17 (2007), pp. 2632–2634. DOI: 10.1364/OL.32.002632.
- [10] Mohammad-Ali Miri and Andrea Alù. “Exceptional points in optics and photonics”. In: *Science* 363.6422 (Jan. 2019), eaar7709. ISSN: 0036-8075. DOI: 10.1126/science.aar7709.
- [11] Şahin Kaya Özdemir et al. “Parity–time symmetry and exceptional points in photonics”. In: *Nature Materials* 18.8 (2019), pp. 783–798. DOI: 10.1038/s41563-019-0304-9.
- [12] Liang Feng, Ramy El-Ganainy, and Li Ge. “Non-Hermitian photonics based on parity–time symmetry”. In: *Nature Photonics* 11.12 (Nov. 2017), pp. 752–762. ISSN: 1749-4893. DOI: 10.1038/s41566-017-0031-1.
- [13] Hossein Hodaei et al. “Enhanced sensitivity at higher-order exceptional points”. In: *Nature* 548.7666 (Aug. 2017), pp. 187–191. DOI: 10.1038/nature23280.
- [14] B. Peng et al. “Loss-induced suppression and revival of lasing”. In: *Science* 346.6207 (Oct. 2014), pp. 328–332. DOI: 10.1126/science.1258004.
- [15] Jung-Wan Ryu et al. “Exceptional classifications of non-Hermitian systems”. In: *Communications Physics* 7.1 (Mar. 2024). ISSN: 2399-3650. DOI: 10.1038/s42005-024-01595-9.
- [16] Muhib Ullah and Said Mikki. “Nonreciprocal microwave field transmission in a quantum magnomechanical system controlled by magnetostriction and Kerr nonlinearities”. In: *Physical Review B* 109.21 (June 2024), p. 214303. ISSN: 2469-9969. DOI: 10.1103/physrevb.109.214303.
- [17] Manuel Reisenbauer et al. “Non-Hermitian dynamics and non-reciprocity of optically coupled nanoparticles”. In: *Nature Physics* 20.10 (July 2024), pp. 1629–1635. ISSN: 1745-2481. DOI: 10.1038/s41567-024-02589-8.
- [18] P. Djorwe, Y. Pennec, and B. Djafari-Rouhani. “Exceptional Point Enhances Sensitivity of Optomechanical Mass Sensors”. In: *Physical Review Applied* 12.2 (Aug. 2019), p. 024002. DOI: 10.1103/PhysRevApplied.12.024002.
- [19] Xi-guang Wang, Guang-hua Guo, and Jamal Berakdar. “Enhanced Sensitivity at Magnetic High-Order Exceptional Points and Topological Energy Transfer in Magnonic Planar Waveguides”. In: *Physical Review Applied* 15.3 (Mar. 2021), p. 034050. DOI: 10.1103/PhysRevApplied.15.034050.
- [20] Tamar Goldzak, Alexei A. Mailybaev, and Nimrod Moiseyev. “Light Stops at Exceptional Points”. In: *Physical Review Letters* 120.1 (Jan. 2018), p. 013901. DOI: 10.1103/PhysRevLett.120.013901.
- [21] P. Djorwé, Y. Pennec, and B. Djafari-Rouhani. “Self-organized synchronization of mechanically coupled resonators based on optomechanics gain-loss balance”. In: *Physical Review B* 102.15 (Oct. 2020), p. 155410. DOI: 10.1103/PhysRevB.102.155410.
- [22] Daniel Hey and Enbang Li. “Advances in synthetic gauge fields for light through dynamic modulation”. In: *Royal Society Open Science* 5.4 (Apr. 2018), p. 172447. ISSN: 2054-5703. DOI: 10.1098/rsos.172447.
- [23] S. R. Mbokop Tchounda et al. “Sensor Sensitivity Based on Exceptional Points Engineered via Synthetic Magnetism”. In: *Physical Review Applied* 19.6 (June 2023), p. 064016. ISSN: 2331-7019. DOI: 10.1103/physrevapplied.19.064016.
- [24] Guan hao Huang et al. “Room-temperature quantum optomechanics using an ultralow noise cavity”. In: *Nature* 626.7999 (Feb. 2024), pp. 512–516. ISSN: 1476-4687. DOI: 10.1038/s41586-023-06997-3.
- [25] Matt Eichenfield et al. “A picogram-and nanometre-scale photonic-crystal optomechanical cavity”. In: *Nature* 459.7246 (May 2009), pp. 550–555. ISSN: 1476-4687. DOI: 10.1038/nature08061.
- [26] B. J. Lawrie et al. “Quantum Sensing with Squeezed Light”. In: *ACS Photonics* 6.6 (May 2019), pp. 1307–1318. ISSN: 2330-4022. DOI: 10.1021/acsp Photonics.9b00250.
- [27] Kejie Fang et al. “Generalized non-reciprocity in an optomechanical circuit via synthetic magnetism and reservoir engineering”. In: *Nature Physics* 13.5 (Jan. 2017), pp. 465–471. ISSN: 1745-2481. DOI: 10.1038/nphys4009.

- [28] Hengjiang Ren et al. “Topological phonon transport in an optomechanical system”. In: *Nature Communications* 13.1, 3476 (June 2022), p. 3476. ISSN: 2041-1723. DOI: 10.1038/s41467-022-30941-0.
- [29] Karl Pelka et al. “Floquet Control of Optomechanical Bistability in Multimode Systems”. In: *Physical Review Letters* 129.12 (Sept. 2022), p. 123603. ISSN: 1079-7114. DOI: 10.1103/physrevlett.129.123603.
- [30] Gui-Lei Zhu et al. “Cavity optomechanical chaos”. In: *Fundamental Research* 3.1 (Jan. 2023), pp. 63–74. ISSN: 2667-3258. DOI: 10.1016/j.fmre.2022.07.012.